

Two-phase solid–liquid coexistence of Ni, Cu, and Al by molecular dynamics simulations using the modified embedded-atom method

Ebrahim Asadi,^{a,*} Mohsen Asle Zaeem,^{a,*} Sasan Nouranian^b and Michael I. Baskes^c

^a*Department of Materials Science and Engineering, Missouri University of Science and Technology, Rolla, MO 65409, USA*

^b*Department of Chemical Engineering, The University of Mississippi, University, MS 38677, USA*

^c*Department of Aerospace Engineering, Mississippi State University, Mississippi State, MS 39762, USA*

Received 30 September 2014; revised 24 November 2014; accepted 7 December 2014

Available online 5 January 2015

Abstract—The two-phase solid–liquid coexisting structures of Ni, Cu, and Al are studied by molecular dynamics (MD) simulations using the second nearest-neighbor (2NN) modified-embedded atom method (MEAM) potential. For this purpose, the existing 2NN-MEAM parameters for Ni and Cu were modified to make them suitable for the MD simulations of the problems related to the two-phase solid–liquid coexistence of these elements. Using these potentials, we compare calculated low-temperature properties of Ni, Cu, and Al, such as elastic constants, structural energy differences, vacancy formation energy, stacking fault energies, surface energies, specific heat and thermal expansion coefficient with experimental data. The solid–liquid coexistence approach is utilized to accurately calculate the melting points of Ni, Cu, and Al. The MD calculations of the expansion in melting, latent heat and the liquid structure factor are also compared with experimental data. In addition, the solid–liquid interface free energy and surface anisotropy of the elements are determined from the interface fluctuations, and the predictions are compared to the experimental and computational data in the literature.

© 2014 Acta Materialia Inc. Published by Elsevier Ltd. All rights reserved.

Keywords: Molecular dynamics; MEAM; Solid–liquid; Melting; Solidification

1. Introduction

Microstructural features, such as grains, phases, dislocations and defects, determine the properties of metals. In metals as well as many other materials, the solidification or crystallization is the initial step of the microstructure formation, and a thorough understanding of the physics of solid–liquid coexistence is a key factor in determining the mechanisms controlling the microstructural features of the material. The experimental study of the phenomena related to the coexistence of solid–liquid structures is generally challenging, because the measurements have to be done at the melting points of the materials. Thanks to recent improvements in computational power and supercomputing capabilities, many research and industrial institutions have started to utilize computational materials modeling as a suitable alternative to costly and/or impractical experiments. Molecular dynamics (MD) simulation and phase-field modeling (PFM), including phase-field crystal (PFC), are the main techniques commonly used to study the solidification and solid–liquid coexistence of different materials [1]. PFM is an efficient computational technique in the

mesoscale for modeling solidification and polycrystalline problems [2–4], and PFC is a new generation of PFM with atomistic details, directly derived from density functional theory [5–7]. On the other hand, MD is a well-developed computational method with great accuracy that can track individual atoms and their energies at smaller length and time scales. In addition, the MD simulations of solid–liquid coexistence of materials can be used to determine many material properties, such as melting point, liquid structure factor, solid and liquid densities, solid–liquid interface free energy and surface anisotropy. These properties provide valuable insights in understanding the material solidification processes. They can also be used to determine the PFC and PFM model parameters, and test the accuracy of these models in simulating the nano- and microstructures resulting from solidification [7–10]. Therefore, the MD modeling of coexisting solid–liquid structures is a very important aspect in investigating the solidification phenomenon.

In MD simulations, choosing a proper technique for modeling the two-phase solid–liquid coexistence of material to calculate the target properties, such as solid–liquid interface free energy, is of critical importance [11]. The major MD simulation techniques to calculate the solid–liquid interface free energy and surface anisotropy are the cleaving technique, critical nucleus method (CNM) and capillary

* Corresponding authors. Tel.: +1 573 341 7184; fax: +1 573 341 6934; e-mail addresses: asadie@mst.edu; zaeem@mst.edu

fluctuation method (CFM). The cleaving technique, which was first used by Broughton and Gilmer [12] and further developed by Davidchack and Laird [13,14], is based on performing multiple steps of MD calculations at the triple points of elemental systems and introducing a cleaving potential to form the solid–liquid interface. CNM is a technique based on determining the critical solid nucleus radius from the Gibbs free energy and comparing it to the MD calculations to find the melting point, and form a coexisting solid–liquid structure. Although calculating the solid–liquid interface free energy by the CNM is a relatively straightforward task, this method has not been utilized yet to determine the solid–liquid interface anisotropy [15–18]. The CFM is based on equilibrating a coexisting solid–liquid structure at the exact melting point of the element, determining the location of the solid–liquid interface, finding the Fourier modes of the solid–liquid interface and using them to determine the solid–liquid interface stiffness [19–23]. Since interface stiffness is more anisotropic than interface free energy, the CFM results in a good prediction of surface anisotropy. However, the CFM typically requires a higher number of atoms than other methods for running the simulations, and the criterion to determine the location of the solid–liquid interface is of key importance in calculating the interface properties. In this study, the CFM technique is utilized, and an improved order parameter is defined to determine the location of the solid–liquid interface.

The capability and accuracy of MD simulations in modeling a phenomenon, like the two-phase solid–liquid coexistence, also depend on the choice of the interatomic potential and its parameters for specific materials and applications. Lennard-Jones (LJ) [12,24], hard-sphere [25–27], Finnis–Sinclair (FS) [16,18], Sutton–Chen [28,29] and embedded-atom methods [20–22,30] are the most commonly used interatomic potentials to investigate the two-phase solid–liquid coexistence of metals. The embedded-atom method (EAM) [31–33] is a semi-empirical many-body potential for the atomistic simulations of metallic systems. The modified embedded-atom method (MEAM) [34,35] was introduced to include the directionality of bonding in covalent materials in the EAM formalism. Today, the MEAM potential is widely used in the computational materials science and engineering community to simulate unary, binary, ternary and multi-component metallic systems with microstructural features, such as grain boundaries, defects, free surfaces, etc. The MEAM formalism reproduces successfully the physical properties of face-centered cubic (fcc) [36–38], body-centered cubic (bcc) [39], hexagonal close-packed (hcp) [40,41] and diamond cubic [42] crystal structures in many lower order (unary, binary, and ternary) and higher order [43] metallic systems. Recently, a MEAM parameter set for Fe was developed by Asadi et al. [8,44] and used to simulate the two-phase solid–liquid coexistence in this bcc metal. Not only did the developed MEAM potential result in reasonable predictions of low-temperature Fe properties, such as elastic constants, surface energies, vacancy formation energy and thermal properties, but it also was successful in predicting the two-phase solid–liquid coexistence properties, such as melting point, latent heat, expansion in melting, liquid structure factor, solid–liquid interface free energy and surface anisotropy. The two-phase solid–liquid coexistence of the fcc metals, such as Ni, Cu, and Al, have never been investigated by MD simulations using the

MEAM potential before, and there are no existing MEAM parameter sets for the fcc metals that are specifically developed for studying solidification in these materials.

In this paper, the second nearest-neighbor (2NN) MEAM parameter sets are presented for modeling the two-phase solid–liquid coexistence of Ni, Cu, and Al. These MEAM parameters are utilized for all the MD simulations performed herein. The low-temperature material properties, such as elastic constants, structural energy differences, vacancy formation energy, stacking fault energies, surface energies, specific heat and thermal expansion coefficient are calculated and compared to the experimental data. In addition, the melting point, expansion in melting, latent heat and liquid structure factor are calculated using the solid–liquid coexistence approach [21], and the results are compared to the experimental and computational data in the literature. In order to determine the solid–liquid interface free energy and surface anisotropy by the CFM, an improved order parameter is defined to locate the solid–liquid interface. These properties are compared with their available counterparts in the literature to verify the accuracy of the current calculations. Wherever it is appropriate, the simulations are repeated in different crystallographic directions with different numbers of atoms to verify the size and orientation independence of the calculated results.

2. MEAM

In this section, we present a brief review of the MEAM formalism and the procedure that we adopted to modify the existing MEAM parameter sets for Ni and Cu. Next, we use the modified MEAM parameters for Ni and Cu and the existing MEAM parameters for Al in MD simulations to calculate the low-temperature properties, melting point and liquid structure factor of these metals. Validating these properties with the experimental data provides confidence in using these MEAM parameters for the MD simulations of two-phase solid–liquid coexistence in Ni, Cu, and Al. The results are presented in Section 3.

2.1. MEAM formalism

In the MEAM formalism [35], the total energy of a unary system is given by

$$E_{tot} = \sum_i \left[F(\bar{\rho}_i) + \frac{1}{2} \sum_{j(\neq i)} S_{ij} \phi(R_{ij}) \right] \quad (1)$$

where F is the “embedding energy” function (energy required to embed an atom in the background electron density $\bar{\rho}_i$ at site i), S_{ij} is the screening factor between atoms at sites i and j [35,45] and ϕ is the pair interaction between atoms at sites i and j with a separation distance of R_{ij} . The embedding function is given by

$$F(\bar{\rho}_i) = \begin{cases} AE^0 \frac{\bar{\rho}_i}{\bar{\rho}^0} \left(\ln \frac{\bar{\rho}_i}{\bar{\rho}^0} \right) & \text{if } \bar{\rho}_i \geq 0 \\ -AE^0 \frac{\bar{\rho}_i}{\bar{\rho}^0} & \text{if } \bar{\rho}_i < 0 \end{cases}, \quad (2)$$

where A is an arbitrary scaling factor, E^0 is the cohesive energy and $\bar{\rho}^0$ is the background electron density for the atom at site i in its reference (typically equilibrium) structure. For the computational convenience, the analytic continuation of the embedding function for negative electron

densities is also considered. This ensures that a system does not enter an unphysical regime. The background electron density $\bar{\rho}_i$ is composed of spherically symmetric ($\rho_i^{(0)}$) and angular ($\rho_i^{(1)}$, $\rho_i^{(2)}$ and $\rho_i^{(3)}$) partial electron densities:

$$\begin{aligned}\rho_i^{(0)} &= \sum_{j \neq i} S_{ij} \rho_j^{a(0)}(R_{ij}), \\ (\rho_i^{(1)})^2 &= \sum_{\alpha} \left[\sum_{j \neq i} \frac{R_{ij}^{\alpha}}{R_{ij}} S_{ij} t^{(1)} \rho_j^{a(1)}(R_{ij}) \right]^2 \rho_i^{(0)} / Q^k, \\ (\rho_i^{(2)})^2 &= \left\{ \sum_{\alpha, \beta} \left[\sum_{j \neq i} \frac{R_{ij}^{\alpha} R_{ij}^{\beta}}{R_{ij}^2} S_{ij} t^{(2)} \rho_j^{a(2)}(R_{ij}) \right]^2 \right. \\ &\quad \left. - \frac{1}{3} \left[\sum_{j \neq i} S_{ij} t^{(2)} \rho_j^{a(2)}(R_{ij}) \right]^2 \right\} \rho_i^{(0)} / Q^k, \\ (\rho_i^{(3)})^2 &= \left\{ \sum_{\alpha, \beta, \gamma} \left[\sum_{j \neq i} \frac{R_{ij}^{\alpha} R_{ij}^{\beta} R_{ij}^{\gamma}}{R_{ij}^3} S_{ij} t^{(3)} \rho_j^{a(3)}(R_{ij}) \right]^2 \right. \\ &\quad \left. - \frac{3}{5} \sum_{\alpha} \left[\sum_{j \neq i} \frac{R_{ij}^{\alpha}}{R_{ij}} S_{ij} t^{(3)} \rho_j^{a(3)}(R_{ij}) \right]^2 \right\} \rho_i^{(0)} / Q^k, \quad (3)\end{aligned}$$

where $Q^k = \sum_{j \neq i} S_{ij} t^{(k)} \rho_j^{a(0)}(R_{ij})$, $k = 1, 2, 3$ and $\rho_j^{a(h)}(h = 0, 1, 2$ and $3)$ are the atomic electron densities at site j at distance R_{ij} from site i . R_{ij}^{α} , R_{ij}^{β} and R_{ij}^{γ} represent the α , β and γ components of the distance vector between atoms at sites i and j , respectively, and $t^{(h)}(h = 1, 2$ and $3)$ are adjustable element-dependent parameters. The MEAM potential utilizes two formalisms for the calculation of many-body interactions: the first nearest-neighbor (1NN) [35] and the 2NN [39]. In the 2NN formalism, the summations in Eq. (3) for the computations of partial electron densities are extended to the 2NN atoms. The partial electron densities are combined using an arbitrary expression involving adjustable element-dependent parameters $t^{(h)}(h = 1, 2$ and $3)$:

$$\begin{aligned}\bar{\rho}_i &= \frac{2\rho_i^{(0)}}{1 + e^{-\Gamma_i}}, \quad \Gamma_i = \sum_{h=1}^3 t_i^{(h)} \left[\frac{\rho_i^{(h)}}{\rho_i^{(0)}} \right]^2, \quad \bar{t}_i^{(h)} \\ &= \frac{1}{\rho_i^{(0)}} \sum_{j \neq i} t_i^{(h)} \rho_j^{a(0)} S_{ij}, \quad (4)\end{aligned}$$

where the atomic electron density is $\rho^{a(h)}(R) = \rho^0 e^{-\beta^{(h)} \left(\frac{R}{R^0} - 1 \right)}$, $\beta^{(h)}(h = 0, 1, 2$ and $3)$ are adjustable element-dependent parameters and R^0 is the nearest-neighbor distance in the equilibrium reference structure.

In this work, the pair interaction is calculated using the 2NN formalism, which is given by

$$\phi(R) = \frac{2}{Z^0} \{E^u(R) - F[\bar{\rho}^{ref}(R)]\}. \quad (5)$$

In this equation, $\bar{\rho}^{ref}(R)$ is the background electron density in the reference structure evaluated from Eq. (4) at a nearest-neighbor distance of R , and $E^u(R)$ is the energy per atom taken from the universal equation of state (UEOS) of Rose et al. [46], given by

$$E^u(R) = -E^0 \left[1 + a^* + \delta \frac{R^0}{R} (a^*)^3 \right] e^{-a^*}, \quad (6)$$

where

$$a^* = \alpha^0 \left(\frac{R}{R^0} - 1 \right), \quad \delta = \begin{cases} \delta^r & \text{if } a^* < 0 \\ \delta^a & \text{if } a^* \geq 0 \end{cases},$$

$$\alpha^0 = \sqrt{\frac{9K^0 \Omega^0}{E^0}}, \text{ for three-dimensional (3D) crystal,}$$

$$\alpha^0 = \sqrt{\frac{k^0}{E^0}} R^0, \text{ for diatomic.} \quad (7)$$

In the above equations, $K^0(k^0)$ and Ω^0 are the bulk modulus (spring constant) and the atomic volume of the reference structure, respectively, and δ is an adjustable element-dependent parameter that has two components, repulsive δ^r and attractive δ^a . Considering the 2NN interactions, the UEOS can be written as

$$E^u(R) = F[\bar{\rho}^{ref}(R)] + \frac{Z_1}{2} \phi(R) + \frac{Z_2 S}{2} \phi(aR), \quad (8)$$

where Z_1 and Z_2 are the number of 1NN and 2NN atoms, respectively, and a is the ratio between the 2NN and 1NN distances. S and a are constants for a given value of C_{min} . Now, the background electron density in the reference structure $\bar{\rho}^{ref}(R)$ is calculated as a function of 1NN distance R by

$$\bar{\rho}^{ref}(R) = Z_1 \rho^{a(0)}(R) + Z_2 S \rho^{a(0)}(aR), \quad (9)$$

where $\rho^{a(0)}(R)$ is the atomic electron density. Eq. (8) can be written as

$$E^u(R) = F[\bar{\rho}^{ref}(R)] + \frac{Z_1}{2} \psi(R), \quad (10)$$

where $\psi(R) = \phi(R) + (Z_2 S / Z_1) \phi(aR)$. Therefore, the pair potential $\phi(R)$ is calculated from

$$\phi(R) = \psi(R) + \sum_{n=1}^N (-1)^n \left(\frac{Z_2 S}{Z_1} \right)^n \psi(a^n R). \quad (11)$$

In this equation, the summation is performed until the correct value of the energy is obtained for the equilibrium reference structure.

The only thing left unknown in the MEAM formalism is the screening function, which is defined as $S_{ij} = \prod_{k \neq i, j} S_{ikj}$, where the interaction between atoms at sites i and j are screened by neighboring atoms at site k . If all three sites i , j and k lie on an ellipse in the xy plane with sites i and j on the x -axis, the following equation results:

$$x^2 + \frac{1}{C} y^2 = \left(\frac{1}{2} R_{ij} \right)^2 \quad (12)$$

where $C_{ikj} = [2(X_{ik} + X_{kj}) - (X_{ik} - X_{kj})^2 - 1] / [1 - (X_{ik} - X_{kj})^2]$, $X_{ik} = (R_{ik} / R_{ij})^2$ and $X_{kj} = (R_{kj} / R_{ij})^2$. The screening factor S_{ikj} for the atoms is defined as

$$S_{ikj} = f_c \frac{C_{ikj} - C_{min}(i, k, j)}{C_{max}(i, k, j) - C_{min}(i, k, j)}, \quad (13)$$

where $C_{min}(i, k, j)$ and $C_{max}(i, k, j)$ determine the extent of screening of atoms at sites i and j by an atom at site k . The smooth cutoff function f_c is defined as

$$f_c(x) = \begin{cases} 1 & x \geq 1 \\ \left[1 - (1 - x)^4 \right]^2 & 0 < x < 1, \\ 0 & x \leq 0 \end{cases} \quad (14)$$

where $S_{ij} = 1$ means that the interaction between atoms at sites i and j is not screened. $S_{ij} = 0$ means the interaction is completely screened.

2.2. MEAM parameters for Ni, Cu, and Al

In this work, we used the 2NN parameters developed by Lee et al. [36] for Ni, Cu, and Al as the starting point and modified the Ni and Cu parameters to better predict the melting points of these fcc metals, which are calculated by the coexistence approach (explained in Section 3.1). We did not change the parameters for Al because the calculated melting point reported by Lee and coworkers was very close to the experimental value; however, we calculated the melting point of Al using the coexistence approach and report it in this work.

During the parameterization of the MEAM potentials for Ni and Cu, we carefully monitored the changes in the physical properties of these materials which resulted from changes made to the MEAM parameters. We strived to make sure that the MEAM predictions of these properties were not deviating noticeably from the experimental data. The final set of parameters for Ni, Cu, and Al are given in Table 1. In this table, the values in bold indicate the modified MEAM parameters for the fcc elements in this work. As mentioned above, we did not modify the MEAM parameters for Al, and used those reported by Lee et al. [36]. For all the calculations and simulations, a cut-off value of 4.0 Å was used for Ni and Cu, while a value of 4.5 Å was employed for Al, all in accordance with the values reported in the work of Lee et al. [36]. Among the 15 parameters listed in Table 1, A and $t^{(3)}$ have the greatest influence on the melting point of all three fcc metals. The α^0 parameter was modified to improve the prediction of other physical properties. In general, the parameter–property relationship is complicated and one cannot easily relate one property to one parameter. However, as pointed out by Lee and coworkers, the effects of some parameters can be confined to a select few properties, and therefore the evalua-

tion of parameters can be done systematically. We performed this systematic evaluation of the effect of MEAM parameters on a single property, i.e., melting point. The challenge was to ensure that our modification of the MEAM parameters for the fcc elements would not deteriorate the other physical properties. Through a series of evaluations, we determined that modifying only A and $t^{(3)}$ would fulfill our main objective to predict the melting point within 3% of the experimental value. However, we had to modify the α^0 parameter to improve the prediction of other physical properties that suffered from our modification to the original MEAM parameters for these elements. The parameter A is the scaling factor of the whole embedding function in Eq. (2). The parameters $t^{(1)}$ and $t^{(3)}$ are the coefficients of \cos and \cos^3 dependent partial electron densities. Therefore, it can be concluded that the amount of the asymmetric background electron density mostly controls the melting point in the MEAM potential.

2.3. 0 K Properties

The calculated physical properties of Ni, Cu, and Al at 0 K are given in Tables 2–4. In Table 2, the calculated bulk modulus B and elastic constants C_{11} , C_{12} and C_{44} are presented for the fcc structure. The calculated values in this work are within 5% error with respect to the experimental data. The calculated point defect and structural energy differences are given in Table 3, where MEAM slightly underpredicts the relaxed vacancy formation energy for Cu and Ni compared with the experimental data. However, the data in Table 3 do not deviate much from the calculated values by Lee et al. [36]. Table 4 summarizes the calculated generalized stacking fault (GSF) energies and surface energies of the fcc metals and their counterpart experimental values. Both unstable and stable GSF energies are given in this table and comparisons are made between the MEAM-calculated values and a range of GSF energy values reported by various literature sources [47]. The stable generalized stacking fault energies (E_{sf}) were calculated

Table 1. 2NN MEAM parameters for Ni, Cu, and Al. E^0 (eV) is the cohesive energy; R^0 (Å) is the nearest neighbor distance in the equilibrium reference structure; α^0 is the exponential decay factor for the UEOS of Rose et al. [46]; A is the electron density scaling factor for the embedding function; ρ^0 is the electron density scaling factor; δ^a and δ^r are the attraction ($a^* > 0$) and repulsion ($a^* \leq 0$) cubic terms for the universal equation of state; $\beta^{(0-3)}$ are the exponential decay factors for the atomic electron densities; $t^{(1-3)}$ are the weighting parameters for the atomic electron densities; and C_{min} and C_{max} are the screening parameters.

	E^0	R^0	α^0	A	δ^a	δ^r	$\beta^{(0)}$	$\beta^{(1)}$	$\beta^{(2)}$	$\beta^{(3)}$	$t^{(1)}$	$t^{(2)}$	$t^{(3)}$	C_{min}	C_{max}
Ni	4.45	2.49	5.08^a	0.99^b	0.00	0.00	2.56	1.50	6.00	1.50	3.10	1.80	2.20^c	0.81	2.80
Cu	3.54	2.56	5.20^d	0.99^e	0.00	0.00	3.83	2.20	6.00	2.20	2.72	3.04	0.85^f	1.21	2.80
Al	3.36	2.86	4.61	1.16	0.00	0.00	3.20	2.60	6.00	2.60	3.05	0.51	7.75	0.49	2.80

^{a,b,c} Original values from Lee et al. [36] were 4.99, 0.94 and 4.36, respectively.

^{d,e,f} Original values from Lee et al. [36] were 5.11, 0.94 and 1.95, respectively.

Table 2. Calculated bulk modulus B and elastic constants (GPa) of Ni, Cu, and Al.

Element	B		C_{11}		C_{12}		C_{44}	
	MEAM	Exp. ^a	MEAM	Exp. ^b	MEAM	Exp. ^b	MEAM	Exp. ^b
Ni	187.1	187.6	260.2	261.2	150.6	150.8	130.9	131.7
Cu	143.5	142.0	176.8	176.2	126.9	124.9	81.8	81.8
Al	76.4	79.4	111.5	114.3	58.8	61.9	29.5	31.6

^a Ref. [36].

^b Ref. [48].

Table 3. Calculated relaxed vacancy formation energy E_v^f (eV) and structural energy differences ΔE (eV) relative to the fcc structures of Ni, Cu, and Al.

Element	E_v^f		$\Delta E_{FCC \rightarrow BCC}$		$\Delta E_{FCC \rightarrow HCP}$	
	MEAM	Exp.	MEAM	Exp. ^d	MEAM	Exp. ^d
Ni	1.19	1.60 ^c	0.18	0.09	0.011	0.010
Cu	0.91	1.03 ^b	0.07	0.04	0.003	0.006
Al	0.69	0.68 ^a	0.12	0.10	0.03	0.06

^a Ref. [49].^b Ref. [50].^c Ref. [51].^d Ref. [52].**Table 4.** Calculated unstable (E_{us}) and stable (E_{sf}) generalized stacking fault energies (mJ m^{-2}) and surface energies E_{surf} (mJ m^{-2}) of Ni, Cu, and Al. The experimental surface energy values E_{poly}^{expt} are for polycrystalline solids, which are extrapolated from high-temperature experimental data.

Element	E_{us}		E_{sf}		E_{poly}^{expt}	$E_{(100)}$	$E_{(110)}$	$E_{(111)}$
	MEAM	DFT/EAM ^a	MEAM	DFT/EAM ^a		MEAM		
Ni	461	261–405	67	13–183	2240 ^c	1821	1885	1493
Cu	211	158–210	20	27–49	1770 ^c	1299	1323	1051
Al	251	83–213	142	6–170	1085 ^b	855	950	661

^a Ref. [47].^b Ref. [53].^c Ref. [54].**Table 5.** Calculated thermal properties of Ni, Cu, and Al. The listed values are thermal linear expansion coefficient ε ($\times 10^6 \text{ K}^{-1}$), heat capacity C_p ($\text{J mol}^{-1} \text{ K}^{-1}$) and melting point T_M (K).

Element	ε (0–100°C)		C_p (0–100°C)		T_M			
	MEAM ^b	Exp. ^a	MEAM ^b	Exp. ^a		Lee et al. ^c	MEAM ^d	MEAM ^b
Ni	11.18	13.30	25.32	26.50	2013		1998	1742
Cu	14.76	17.00	25.30	24.50	1602		1552	1320
Al	17.31	23.50	26.15	24.70	937		925	925

^a Ref. [55].^b Present work.^c Ref. [36].^d Calculated using parameters reported in Ref. [36].^e Refs. [55–58].

using the original MEAM parameters by Lee and coworkers as 125, 42 and 141 for Ni, Cu, and Al, respectively. The modifications of the MEAM parameters for Ni and Cu reduce E_{sf} by 46% and 52%, respectively. The calculated surface energies in various planes are compared with the surface energies associated with polycrystalline solids, which are extrapolated from room-temperature experimental data (Table 4).

2.4. Thermal properties

The calculated thermal properties of Ni, Cu, and Al are compared with their experimental counterparts in Table 5. Thermal linear expansion coefficient ε and heat capacity C_p are calculated for 0–100°C temperature change. The coexistence approach is utilized to calculate the melting points of the fcc metals with the original MEAM parameters of Lee et al. [36] as well as the modified MEAM parameters in this work. The detail of the calculations and more discussion on the melting properties will be provided in Section 3.1. Our calculated values utilizing the modified MEAM parameters are 15.6%, 21.4% and 0.7% lower than the reported values

by Lee and coworkers for Ni, Cu, and Al, respectively. In summary, the results presented in this section verify that the modification of the MEAM parameters in this work improves the melting point predictions of Ni and Cu comparing to the experiments, while we have not compromised the prediction of low-temperature and thermal properties of these elements by our modifications.

2.5. Liquid structure factor

In all the simulations reported hereafter, the large-scale atomic/molecular massively parallel simulator (LAMMPS) MD code [59] with the time step size of 0.002 ps is used. The boundary conditions are periodic in all three directions. Also, we utilized the 2NN-MEAM interatomic potential with parameters provided in Table 1 for the MD simulations. Wherever heating/cooling of the simulation box is required, the heating/cooling time from the initial temperature to the target temperature is 2.5 ps; this choice results in a reasonable time for the target temperature equilibration, and produces reasonable fluctuations of the equilibrated temperature in all the simulations.

The first step in calculating the liquid structure factor $S(k)$ for Ni, Cu, and Al is to calculate the radial distribution function $g(r)$ of the liquid phase at the melting point of each element. In order to calculate $g(r)$, a simulation box consisting of $20 \times 20 \times 20$ lattice cells was melted and equilibrated for 0.5 ns at the calculated melting points of the elements.

The zero pressure condition was applied in all directions. The time-averaged $g(r)$ was calculated over 0.5 ns for the distance of 20.0 Å. The calculated $g(r)$ for Ni, Cu, and Al along with the experimental measurements from Ref. [60] are shown in Fig. 1a–c, respectively. In general, the MEAM-MD predictions of $g(r)$ for all the considered elements are in very good agreement with the experimental data, especially for the location and height of the peaks, except for the height of the first peaks. A small deviation from the experimental data is noticeable in the MEAM-MD predictions of the height of the first peak, especially for Ni; these deviations from the experimental values for Ni, Cu, and Al are 23%, 3% and 3%, respectively.

The structure factor of an element can be calculated by applying a Fourier transform to its radial distribution function through the following equations:

$$S(k) = 1 + 4\pi\rho_l \int_0^R r^2 [g(r) - 1] \frac{\sin(kr)}{kr} \frac{\sin(\pi r/R)}{\pi r/R} dr, \\ k < k_{\min}, \\ S(k) = 1 + 4\pi\rho_l \int_0^R r^2 [g(r) - 1] \frac{\sin(kr)}{kr} dr, \quad k > k_{\min}, \quad (15)$$

where R is the half of the size of the simulation box, and the $\sin(\pi r/R)/(\pi r/R)$ term is called the window function [61]. The window function filters the fluctuations of the structure factor at small waves and hence it should only be used for these waves. Utilizing the window function for larger k tends to decrease the values of the peaks in the structure factor, especially the value of the first peak. Therefore, the window function was used to calculate $S(k)$ for $k < k_{\min}$, where k_{\min} is a value smaller than the location of the first peak. The calculated radial distribution functions for each element were substituted into Eq. (15) and the resulting integrals were calculated numerically for different k values to determine the liquid structure factor of the element. The calculated liquid structure factors of Ni, Cu, and Al along with their experimental counterparts are shown in Fig. 1d–f, respectively. The calculated liquid structure factors for all the elements match reasonably well with the experiments, except for the height of the first peak, where a slight difference is noticeable; there are 9%, 2% and 6% deviations from the experiments for Ni, Cu, and Al, respectively. In addition, an alternative experimental liquid structure factor for Ni, Cu, and Al is presented in Fig. 1d–f by green solid curves. The alternative $S(k)$ are calculated by substituting the experimental $g(r)$ of the elements into Eq. (15). The MEAM-MD calculations of the liquid structure factor match the alternative experimental curves, even for the height of the first peaks (2%, 11% and 0% error for Ni, Cu, and Al, respectively) except for the height of the first peak for Cu. The reason for this error might be the difference in the temperatures where the experiments were measured and where the MEAM-MD calculations were performed (3%, 5% and 2% differences for Ni, Cu, and Al, respectively). It is also worth mentioning that the

MEAM-MD calculations of $g(r)$ and $S(k)$ are pure predictions since they were not included in the fitting database for the potential parameterization.

3. Two-phase solid–liquid coexistence of Ni, Cu, and Al

The modified and validated MEAM parameters in the preceding section were utilized to model the two-phase solid–liquid coexisting structures of Ni, Cu, and Al. First the solid–liquid coexistence approach that we utilized to calculate the melting point is explained. Then, the calculated melting point, expansion in melting and latent heat of the elements are compared with their experimental counterparts as another validation step. In Sections 3.2 and 3.3, we explain and discuss the CFM [26,62] used to determine the solid–liquid interface fluctuations, interface free energy and surface anisotropy.

3.1. Melting properties

The first step to investigate the two-phase solid–liquid coexistence is to determine the exact melting point, T_M , because the MD calculation of the melting point varies significantly depending on which interatomic potential is used in the MD simulations [30]. The exact melting point is calculated by simultaneously equilibrating the solid and liquid phases in a simulation box. In order to construct the two-phase solid–liquid coexisting structure of the elements, a simulation box consisting of $m \times n \times l$ periodic solid cells is equilibrated at an estimated melting point of the material [8], where the l direction is normal to the solid–liquid interface and longer than the other two directions. Then, the central half of the simulation box is melted at a high temperature by running a dynamics simulation using a canonical ensemble (NVT) with a Nöse–Hoover thermostat [63,64], while holding the other half fixed. The melted half of the simulation box is equilibrated at the estimated melting point using an isothermal-isobaric (NPT) ensemble for 0.5 ns, while the box size in the normal direction is allowed to relax, and still holding the other solid half fixed. The entire simulation box is allowed to relax in the normal direction for 1 ns using an NPT ensemble at the estimated melting point (to minimize the pressure in all directions). Finally, the refined value of the melting point is calculated using an isenthalpic ensemble (NPH) simulation lasting for a considerable amount of time (~ 10 ns), while the size of the box in the normal direction is allowed to relax (to minimize the normal pressure). The whole process is repeated using the calculated refined temperature instead of the estimated melting point until convergence is achieved.

We performed a convergence check to determine the dependence of the calculated melting point on the size and orientation of the simulation box for all the three elements. The result of this study is reported in Table 6, where it can be verified that the calculated melting point converges for a simulation box consisting of $\sim 82,000$ atoms. There is less than 0.1% variation in the value of the melting point based on the orientation of the simulation box. This variation can further be minimized if a larger simulation box is chosen. Therefore, we conclude that the calculated melting point is size- and orientation-independent.

The melting point using the modified MEAM parameters is determined as the average value of the calculated

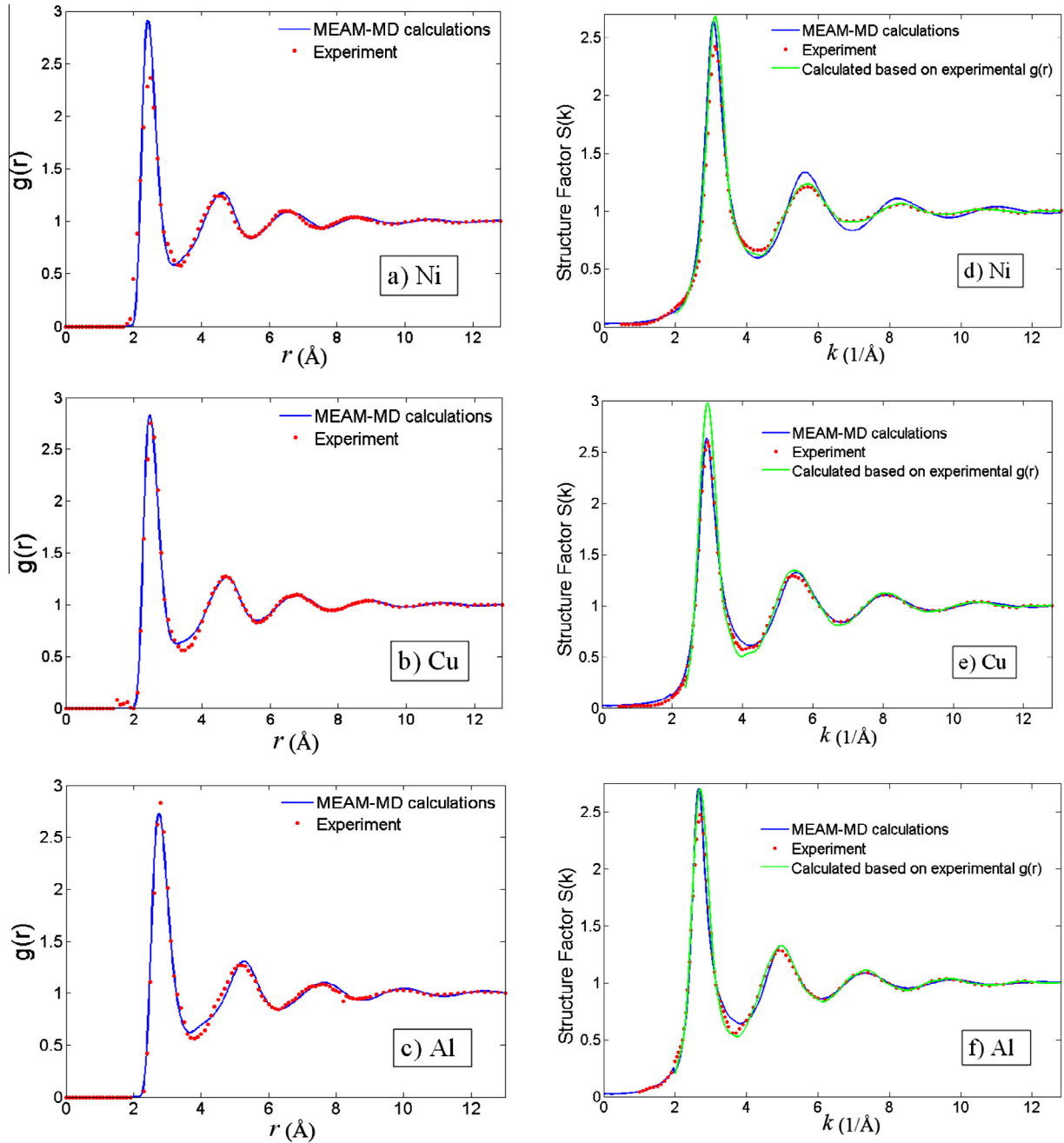


Fig. 1. Radial distribution function $g(r)$ and liquid structure factor $S(k)$ calculated by MEAM-MD simulations at the calculated melting points of the elements (reported in Tables 5 and 7) compared to the experiments reported by Waseda [60]. Experimental measurements were performed at 1773 K, 1423 K and 943 K for Ni, Cu, and Al, respectively. An alternative experimental liquid structure factor based on experimental $g(r)$ is also presented (green curves) by using Eq. (15). (a) $g(r)$ for Ni, (b) $g(r)$ for Cu, (c) $g(r)$ for Al, (d) $S(k)$ for Ni, (e) $S(k)$ for Cu, (f) $S(k)$ for Al. (For interpretation of the references to color in this figure legend, the reader is referred to the web version of this article.)

melting points for the three orientations reported in Table 6. The calculated average melting point (T_M), latent heat (L) and expansion in melting ($\Delta V_{\text{melting}}$) for all the three elements, along with their experimental counterparts, are reported in Table 7. Since the experimental values of the expansion from room temperature to the melting point of the liquid ($\Delta V_{r.t.-\text{liquid}}$) for Ni, Cu, and Al have been more frequently reported in the literature [56,57], as opposed to the experimental values of $\Delta V_{\text{melting}}$ [55], we have followed the same trend and present the calculated values of

$\Delta V_{r.t.-\text{liquid}}$ in Table 7. Our MEAM-MD calculations of the melting point for all the elements may be compared with the experimental values (less than 1% error for Ni and Al, and 2.8% error for Cu). Also, the calculated latent heat by MEAM-MD simulations may be compared with the experimental data for Cu and Al ($\sim 7\%$ error); however, for Ni the amount of error is significantly higher ($\sim 27\%$). The error for the calculated expansion in melting is higher, except for Al, where the error is $\sim 5\%$. The calculated values of $\Delta V_{r.t.-\text{liquid}}$ for Ni and Cu are in better agreement with

Table 6. The calculated melting point, T_M (K), for Ni, Cu, and Al vs. the size and the orientation of the MD simulation box.

Orientation	Size	Atoms	T_M : Ni	T_M : Cu	T_M : Al
$[001] \times [010] \times [001]$	$8 \times 8 \times 96$	24576	1743.6	1321.4	925.3
$[001] \times [010] \times [001]$	$10 \times 10 \times 120$	48000	1743.1	1321.7	925.8
$[001] \times [010] \times [001]$	$12 \times 12 \times 144$	82944	1743.0	1319.8	924.9
$[001] \times [1\bar{1}0] \times [110]$	$12 \times 9 \times 108$	93312	1740.8	1320.2	924.7
$[1\bar{1}0] \times [11\bar{2}] \times [111]$	$9 \times 5 \times 90$	97200	1741.0	1318.8	925.1

Table 7. Comparison of the calculated melting point with the experiment for T_M (K), latent heat L (kJ mol⁻¹), expansion in melting ΔV (Å³ atom⁻¹) and expansion from room temperature to liquid at the melting point $\Delta V_{r.t.-liquid}$ (Å³ atom⁻¹).

	Method	T_M	L	$\Delta V_{melting}$	$\Delta V_{r.t.-liquid}$
Ni	Exp. data ^a	1728.0	17.48	0.54	1.54
	MEAM-MD	1741.6	22.17	1.011	1.66
Cu	Exp. data ^a	1357.8	13.26	0.53	1.38
	MEAM-MD	1319.6	14.21	0.76	1.00
Al	Exp. data ^a	933.5	10.71	1.14	2.27
	MEAM-MD	924.9	11.50	1.08	1.78

^a Refs. [55–58].

the experiments (7% error for Ni and 28% error for Cu). Note that for Ni and Cu the melting point was used in the MEAM parameterization and that the rest of the properties presented in Table 7 are predictions.

3.2. Solid–liquid interface stiffness

To calculate the solid–liquid interface stiffness a slab of two-phase coexisting solid–liquid Ni, Cu, and Al is used. The slab has a thickness of b , a width of W and a length of L (normal to the solid–liquid interface direction), where $b \ll W$. The two-phase solid–liquid coexisting slab is equilibrated at the melting point of each element using the method explained in the preceding section. This slab consists of $m \times n \times l$ lattice cells, where m, n and l are the number of periodic lattice cells along the width, thickness and normal directions, respectively. Since the slab is equilibrated at the exact melting point determined by the modified MEAM parameters for each element, the final NPH simulation took only 240 ps. A snapshot of the atoms' positions was taken every 0.2 ps (total of 1201 frames) and an example of the two-phase coexisting solid–liquid slab is shown in Fig. 2, where the color of the atoms changes from red (liquid) to blue (solid) at the solid–liquid interface. We discuss below how we distinguish the solid and liquid atoms. Since $b \ll W$, the solid–liquid interface $h(x)$ is only a function of position in the width direction (x) and is assumed to be unaffected by the thickness direction. In Fig. 2, two Cartesian coordinate systems denoted by their unit vectors are shown: (I) \hat{z}_1, \hat{z}_2 and \hat{z}_3 , parallel to the $[100]$, $[010]$ and $[001]$ directions, respectively, and (II) $\hat{x}_1 : [a_1b_1c_1]$, $\hat{x}_2 : [a_2b_2c_2]$ and $\hat{x}_3 : [a_3b_3c_3]$, parallel to the periodic directions of the simulation box. For the slab shown in Fig. 2, the element is Cu, $[a_1b_1c_1] = [012]$, $[a_2b_2c_2] = [021]$ and $[a_3b_3c_3] = [100]$; thus the orientation is denoted by $\langle 012 \rangle \{100\}$, which means that \hat{x}_1 is parallel to the $\langle 012 \rangle$ direction and the solid–liquid interface plane is $\{100\}$.

In order to identify an atom as liquid or solid, we define an order parameter, ψ , and calculate it for each atom as

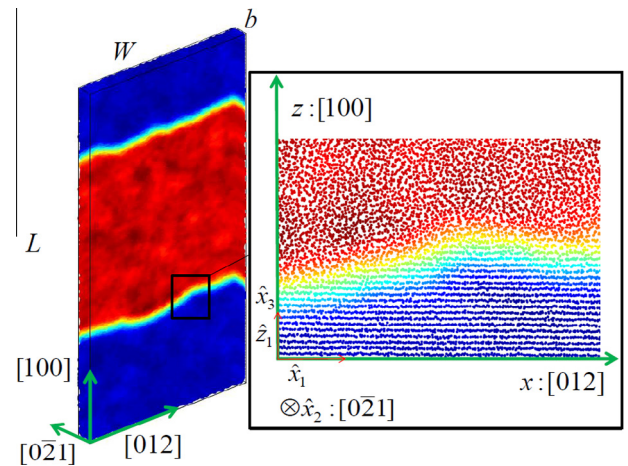


Fig. 2. A snapshot of the two-phase coexisting solid–liquid structure of Cu for $\langle 012 \rangle \{100\}$ orientation. The atoms are colored based on their order parameters, ψ , and the color of the atoms changes from red (liquid) to blue (solid) at the solid–liquid interface. (For interpretation of the references to color in this figure legend, the reader is referred to the web version of this article.)

$$\psi = \sum_i w_d r_i \phi_i / \sum_i w_d r_i, \quad (16)$$

where $w_d = \left[1 - \left(\frac{r_i}{d}\right)^2\right]^2$, $r_i = \sqrt{(x_i - x)^2 + (z_i - z)^2}$, d is the radius of the smoothing cylinder for ψ and the summation is over all the atoms in the smoothing distance $r_i < d$. In Eq. (16), $\phi = (1/12) \sum |\vec{r}_i - \vec{r}_{fcc}|^2$ is the order parameter used by Sun et al. [21], where the summation is over 12 1NNs and \vec{r}_{fcc} denotes the neighbor positions at the perfect fcc lattice. The two order parameters ϕ and ψ are compared in Fig. 3 for a line parallel to the z direction for two different orientations. In this figure, $d = 2L_{fcc}$ for the purpose of calculating ψ , and ϕ is averaged over a cubic lattice cell with the length of L_{fcc} , where L_{fcc} is the lattice parameter of the element (Cu) at its melting point. The definition of the order parameter in Eq. (16) results in a continuous

function with damped oscillations compared to the profile of ϕ , and this makes the identification of the interface location easier. The value of the order parameter is typically small in the solid state (~ 0.13) and larger in the liquid phase (~ 0.28). At the interface location, the order parameter varies from ~ 0.13 to ~ 0.28 , and therefore the interface location is identified as the location where the order parameter takes its average value ($\psi_{\text{int}} \sim 0.20$).

The solid–liquid interface stiffness is defined as $\gamma + d^2\gamma/d\theta^2|_{\theta=0}$, where γ is the solid–liquid interface free energy for a given orientation and θ is the angle between the normal to the interface and the x direction. A relation for the solid–liquid interface stiffness can be derived by utilizing the Fourier modes of the interface, i.e., $A(k)$, and calculating the amount of the energy required to alter the interface from its average value for each mode. The energy equilibration dictates a constant mean energy to be $k_B T_M$ for each Fourier mode [65]. Therefore, the interface energy relation becomes $k_B T_M = b \int \gamma(\theta) ds$, where $ds = \sqrt{1 + (dh/dx)^2}$. By approximating $\theta \approx dh(x)/dx$ and $\sqrt{1 + (dh/dx)^2} \approx 1 + \theta^2/2$, the desired relation for the interface stiffness is obtained as

$$\gamma + d^2\gamma/d\theta^2 = \frac{k_B T_M}{bW \langle |A(k)|^2 \rangle k^2}, \quad (17)$$

where $\langle |A(k)|^2 \rangle$ is the mean square amplitude of the Fourier modes. Therefore, the slope of the $k_B T_M/bW \langle |A(k)|^2 \rangle$ vs. k^2 line is equal to the interface stiffness for the given orientation. In summary, the following steps are taken to calculate the interface stiffness for each element and orientation: (1) the two-phase coexisting solid–liquid slab is constructed, (2) the interface location $h(x)$ is determined from the definition of ψ , (3) the Fourier modes $A(k)$ of the

interface is determined and averaged over all of the frames and both interfaces in the structure (a total of 2402 data sets), (4) a line is fitted to the $k_B T_M/bW \langle |A(k)|^2 \rangle$ vs. k^2 data and (5) the slope of the fitted line is calculated to be the solid–liquid interface stiffness.

We considered five different orientations listed in Table 8. In Fig. 4, the variation of $k_B T_M/bW \langle |A(k)|^2 \rangle$ vs. k^2 for Ni, Cu, and Al are compared for these orientations. A 95%-confidence line is fitted to the data associated with each orientation using the least-squares method, where the slope of the line equals the interface stiffness. Since $k_B T_M/bW \langle |A(k)|^2 \rangle$ does not fall on the fitted line for very large and very small modes (possibly because of the numerical round-off error), a finite number of modes are utilized in the fitting procedure such that the norm of the residuals is less than three. We also performed a convergence check to verify that our stiffness calculations are independent of the smoothing distance and slab thickness. All the stiffness calculations converged for a smoothing distance as large as $d/L_{\text{bcc}} = 2$. Also, the number of the required periodic cells in each direction for convergence is reported in Table 8.

Using a small value for b makes the equilibration of solid–liquid structure challenging. At the same time, using a very large value for b results in the changing of the behavior of the $1/\langle |A(k)|^2 \rangle - k^2$ curve from linear to logarithmic. We list the calculated solid–liquid interface stiffness of Ni, Cu, and Al for all five orientations along with the total number of atoms (120–200 K) in the slab in the last four columns of Table 8.

Two interesting points should be highlighted considering the results shown in Fig. 4 and Table 8. First, the length of the Fourier modes (k^2) that fall onto a line is largest for $\langle 100 \rangle \{001\}$ and $\langle 012 \rangle \{100\}$ orientations in Fig. 4a and d, respectively. It is interesting to observe that these two orientations have the lowest interface stiffness with their

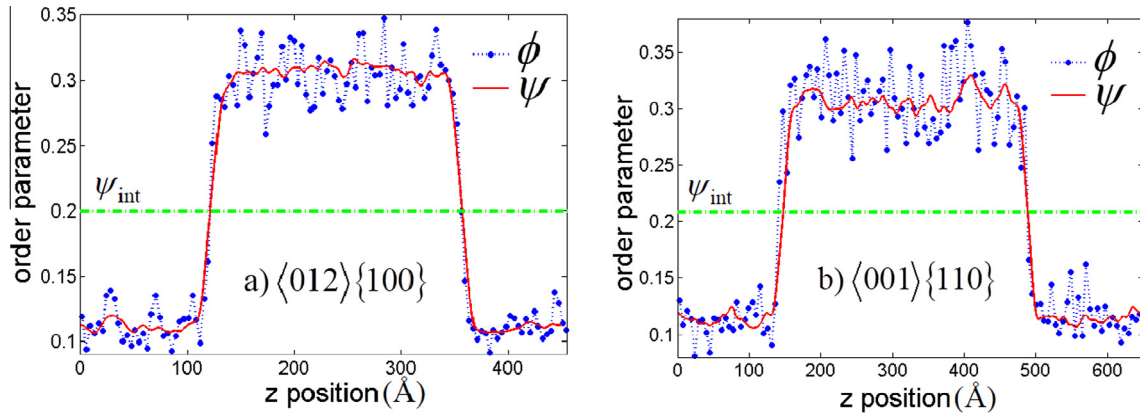


Fig. 3. Plots of the order parameters ϕ and ψ for Cu in the z direction. a) $\langle 012 \rangle \{100\}$ orientation, and b) $\langle 001 \rangle \{110\}$ orientation.

Table 8. The solid–liquid interface stiffness $(\gamma + d^2\gamma/d\theta^2)|_{\theta=0}$ calculated analytically using Eq. (18) and by MEAM-MD simulations for Ni, Cu, and Al.

Orientation	Box size		Expression (Eq. (18))	$\gamma + d^2\gamma/d\theta^2$ (mJ m ⁻²)		
	Periodic cells	Atoms		Ni	Cu	Al
$\langle 100 \rangle \{001\}$	$75 \times 2 \times 210$	126000	$\gamma_0[1 - (18/5)\delta_1 - (80/7)\delta_2]$	265.6	203.5	148.8
$\langle 1\bar{1}0 \rangle \{110\}$	$60 \times 2 \times 180$	172800	$\gamma_0[1 + (39/10)\delta_1 + (155/14)\delta_2]$	406.5	312.2	203.6
$\langle 001 \rangle \{110\}$	$70 \times 2 \times 150$	168000	$\gamma_0[1 - (21/10)\delta_1 + (365/14)\delta_2]$	219.6	189.7	135.2
$\langle 012 \rangle \{100\}$	$35 \times 2 \times 130$	182000	$\gamma_0[1 - (18/5)\delta_1 - (80/7)\delta_2]$	271.8	196.5	145.6
$\langle 1\bar{1}2 \rangle \{110\}$	$35 \times 2 \times 120$	201600	$\gamma_0[1 - (1/10)\delta_1 + (295/14)\delta_2]$	290.9	223.4	163.6

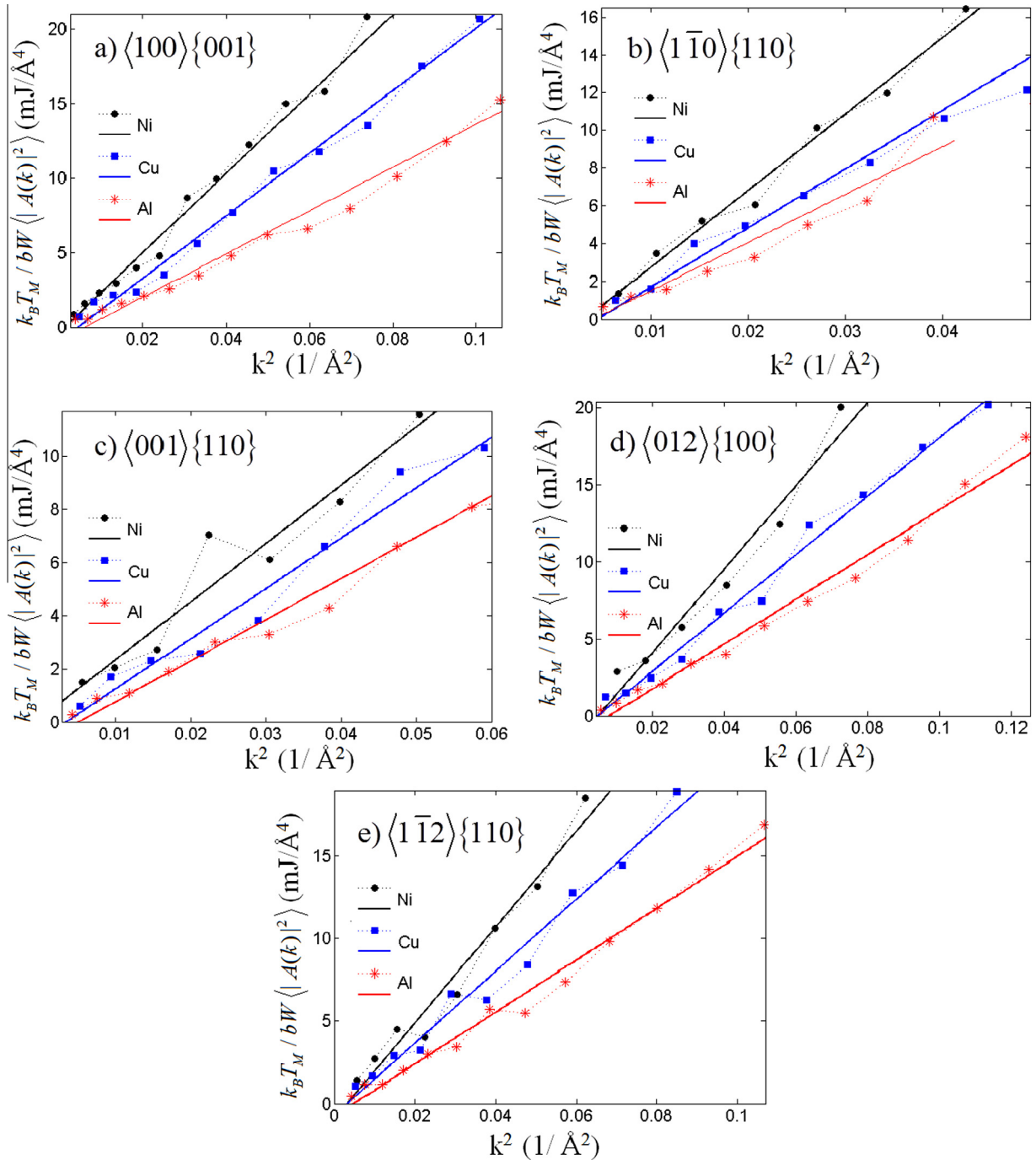


Fig. 4. Plots of $k_B T_M / bW \langle |A(k)|^2 \rangle$ versus k^2 for Ni, Cu, and Al. The solid lines represent the 95%-confidence line for each orientation, where the norm of the fitting residual is less than three for all the cases. (a) $\langle 100 \rangle \{001\}$ orientation, (b) $\langle 1\bar{1}0 \rangle \{110\}$ orientation, (c) $\langle 001 \rangle \{110\}$ orientation, (d) $\langle 012 \rangle \{100\}$ orientation and (e) $\langle 1\bar{1}2 \rangle \{110\}$ orientation.

values being almost equal. Considering the length of the Fourier modes for other directions, we conclude that, as the amount of interface stiffness increases, the length of the Fourier modes that fall onto the fitted line decreases. Second, the interface stiffness of all of the considered orientations for Ni is greater than that of Cu, and the interface stiffness of Cu is greater than that of Al. The results reported in Table 7 verify that the same pattern applies to the melting point and latent heat of these elements. Therefore, there is a direct correlation between the solid–liquid interface stiffness of the elements and their melting

point/latent heat. This observation is in agreement with previous studies of solid–liquid coexistence of fcc metals [28].

3.3. Solid–liquid interface free energy

As shown in the preceding section, the solid–liquid interface stiffness of an element varies for different interfacial orientations. Thus, we expect that the solid–liquid interface free energy be also a function of the direction normal to the interface (\hat{n}). It has been previously shown that $\gamma(\hat{n})$ can be

approximated in terms of its anisotropy using a finite number of spherical harmonics with cubic symmetry [66]. We utilize this concept to determine the solid–liquid interface free energy and its anisotropy for Ni, Cu, and Al. The interface free energy for a given orientation in terms of the first three spherical harmonics can be written as [19,27]

$$\gamma(\hat{n})/\gamma_0 = 1 + \delta_1 \left(\sum_{i=1}^3 n_i^4 - 3/5 \right) + \delta_2 \left(3 \sum_{i=1}^3 n_i^4 + 66n_1^2 n_2^2 n_3^2 - 17/7 \right) \quad (18)$$

where δ_1 and δ_2 are anisotropy parameters, γ_0 is the average interface free energy and $\hat{n} = (n_1, n_2, n_3)$ is the unit vector, which is normal to the solid–liquid interface. In Eq. (18), the first term represents the isotropic portion of the interface free energy. The second and third terms are related to the surface anisotropy with fourfold and sixfold symmetries, respectively. Thus, the parameters δ_1 and δ_2 are also called fourfold and sixfold anisotropy parameters, respectively.

Since the interfacial stiffness is more anisotropic than γ (by an order of magnitude) [19], we utilize its definition to determine the interface free energy and anisotropy parameters. First, we need to derive expressions for the solid–liquid interface stiffness for a given orientation in terms of γ_0 , δ_1 and δ_2 . As we explained in the preceding section, the unit vector normal to the interface is not a function of the interface position at \hat{x}_2 direction because $b \ll W$. Therefore, (n_1, n_2, n_3) can be shown in terms of the angle (θ) between \hat{x}_1 and the interface plane:

$$n_i = (\sin \theta \hat{x}_1 + \cos \theta \hat{x}_3) \cdot \hat{z}_i, \quad i = 1, 2, 3 \quad (19)$$

The relationship between the two sets of unit vectors is $\hat{x}_i = (a_i \hat{z}_1 + b_i \hat{z}_2 + c_i \hat{z}_3) / \sqrt{a_i^2 + b_i^2 + c_i^2}$. The relationship between $\gamma(\hat{n})$ and θ can be obtained by substituting Eq. (19) into Eq. (18) for the desired orientation, and the expressions for the interface stiffness $(\gamma + d^2\gamma/d\theta^2)|_{\theta=0}$ can be determined from $\gamma(\theta)$.

The resulted expressions for the interface stiffness along with their calculated values for Ni, Cu, and Al for the five considered orientations in this study are presented in Table 8. The interface stiffness values were calculated in the preceding section. Since we have three unknown variables in our expressions (γ_0 , δ_1 and δ_2), the expressions for three orientations will be necessary to determine these variables. We will use the other two expressions to check for the corresponding error in approximating the solid–liquid interface free energy by utilizing three spherical harmonics with cubic symmetry in Eq. (18).

We utilized the first three expressions in Table 8, i.e., expressions related to $\langle 100 \rangle \{001\}$, $\langle 1\bar{1}0 \rangle \{110\}$ and $\langle 001 \rangle \{110\}$ orientations, to calculate γ_0 , δ_1 and δ_2 for Ni, Cu, and Al. The calculated results are reported in Table 9. The interface stiffness of the other two orientations ($\langle 012 \rangle \{100\}$ and $\langle 1\bar{1}2 \rangle \{110\}$) are determined by substituting the calculated γ_0 , δ_1 and δ_2 parameters for each element into the related stiffness expressions. These results are compared with the MEAM-MD calculations (the last two rows in Table 8) to check if the approximation used in Eq. (18) is a valid one; the maximum difference for this comparison for all the elements is $\sim 3\%$. This difference is roughly the norm of the residuals used in the line fitting

Table 9. Comparison of the calculated average solid–liquid interface free energy (γ_0), and fourfold (δ_1) and sixfold (δ_2) symmetry anisotropy parameters of Ni, Cu, and Al with the available experimental and computational data in the literature.

Elem.		γ_0 (mJ/m ²)	δ_1 (%)	δ_2 (%)
Ni	MEAM-MD ^a	331.8	7.7	−0.68
	EAM-MD ^b	310.3–284.7	9.0–8.8	−1.1
	Exp. ^c	364	—	—
Cu	MD ^a	255.0	7.0	−0.42
	EAM-MD ^b	195.7	8.1	−1.0
	Exp. ^c	237 ± 26–270	—	—
Al	MD ^a	172.6	5.7	−0.37
	EAM-MD ^b	149.0	—	—
	Exp. ^c	168.9 ± 21–158 ± 30	—	—

^a Present work.

^b Reported at Ref. [11].

^c Refs. [67–69].

when calculating the stiffness (see Fig. 4 and related notes in the preceding section). For example, by substituting the calculated γ_0 , δ_1 and δ_2 parameters into the last expression in Table 8, the interface stiffnesses $\langle 1\bar{1}2 \rangle \{110\}$ are determined to be 281.9, 230.5 and 158.0 for Ni, Cu, and Al, respectively. These values are comparable to the MD calculated ones (290.9, 223.4 and 163.6, respectively). In addition, the expression of stiffness for the $\langle 012 \rangle \{100\}$ orientation is the same as that for the $\langle 100 \rangle \{001\}$; thus, the calculated stiffness for these two orientations for the given element should be the same. Therefore, the use of Eq. (18) to estimate the solid–liquid interface free energy of the considered fcc metals is an appropriate method to express its anisotropy (with $\sim 3\%$ error). The MEAM-MD calculations of both fourfold and sixfold anisotropy parameters for all considered elements are of the same order, because they have the same crystallographic structure (fcc). In Table 9, the average solid–liquid interface free energy (γ_0) and surface anisotropy parameters (δ_1 and δ_2) for Ni, Cu, and Al is compared against experiments and available EAM-MD calculated values in the literature. This comparison shows that our MEAM-MD calculations of γ_0 for all the elements are in good agreement with the experiments. Generally, the MEAM potential predicts higher γ_0 (closer to the experiments) compared to the EAM calculations. However, MEAM-MD calculations yield smaller anisotropy parameters (δ_1 and δ_2) for all the considered elements compared to the EAM-MD calculations.

4. Conclusions

The 2NN MEAM potential was used to run MD simulations and to calculate the low- and high-temperature as well as the two-phase solid–liquid coexistence properties of the fcc metals: Ni, Cu, and Al. We modified the existing parameter sets for Ni and Cu by including the melting point in the potential fitting database along with other physical properties, showing that these modified MEAM parameters for Ni and Cu along with the existing MEAM parameters for Al give reasonable predictions of the properties mentioned above.

Our MEAM-MD calculations of the melting point for Ni, Cu, and Al are 1742 K, 1320 K and 924 K, respectively, and the experimental melting points are 1728 K, 1357 K and 925 K; the maximum error in the calculation of the

melting point was $\sim 2.8\%$ for Cu. In addition, the calculations of low-temperature properties such as elastic constants, structural energy differences, vacancy formation energy, stacking fault energies, surface energies, specific heat and thermal expansion coefficient of Ni, Cu, and Al were in reasonably good agreement with the experimental data and previous MD calculations. The predicted MEAM-MD curves for liquid structure factor matches the experiments; however, a slight deviation was detected in the calculated height of the first peak of the liquid structure factor (9%, 6% and 3% error for Ni, Cu, and Al, respectively).

We defined a new order parameter in the concept of capillary fluctuation method (CFM) to identify atoms as solid or liquid in the two-phase solid–liquid coexistence simulations. The definition of the new order parameter resulted in a continuous order parameter at the normal to the solid–liquid interface direction with damped oscillations, and consequently, a better identification of atoms as solid or liquid during the simulations. The MEAM-MD simulations predicted the average solid–liquid interface free energy (mJ m^{-2}) of Ni, Cu, and Al as 332.8, 255.0 and 172.6, respectively, which are typically higher than EAM-MD calculated ones (310.3–284.7, 195.7 and 149.0 for Ni, Cu, and Al, respectively), but, nevertheless, in agreement with the experimental measurements (364, 237–270 and 168–158 for Ni, Cu, and Al, respectively). Furthermore, MEAM-MD calculations predicted positive fourfold symmetry anisotropy parameter and negative sixfold anisotropy parameter, all in agreement with EAM-MD calculations. However, we observed slightly smaller anisotropies for Ni and Cu compared to the EAM calculations reported in the literature.

Acknowledgment

The authors are grateful for computer time allocation provided by the Extreme Science and Engineering Discovery Environment (XSEDE).

References

- [1] H. Humadi, N. Ofori-Opoku, N. Provatas, J.J. Hoyt, *JOM* 65 (2013) 1103.
- [2] W. Boettinger, J. Warren, C. Beckermann, A. Karma, *Annu. Rev. Mater. Res.* 32 (2002) 163.
- [3] L.-Q. Chen, *Annu. Rev. Mater. Res.* 32 (2002) 113.
- [4] A. Karma, *Phys. Rev. Lett.* 87 (2001) 115701.
- [5] K. Elder, M. Grant, *Phys. Rev. E* 70 (2004) 051605.
- [6] K. Elder, M. Katakowski, M. Haataja, M. Grant, *Phys. Rev. Lett.* 88 (2002) 245701.
- [7] E. Asadi, M.A. Zaeem, *JOM* (2014), In press, <http://dx.doi.org/10.1007/s11837-014-1232-4>.
- [8] E. Asadi, M.A. Zaeem, M.I. Baskes, *JOM* 66 (2014) 429.
- [9] K.-A. Wu, A. Karma, *Phys. Rev. B* 76 (2007) 184107.
- [10] K.-A. Wu, A. Adland, A. Karma, *Phys. Rev. E* 81 (2010) 061601.
- [11] J. Hoyt, M. Asta, A. Karma, *Mater. Sci. Eng. R* 41 (2003) 121.
- [12] J. Broughton, G. Gilmer, *J. Chem. Phys.* 84 (1986) 5759.
- [13] R.L. Davidchack, B.B. Laird, *Phys. Rev. Lett.* 85 (2000) 4751.
- [14] R.L. Davidchack, B.B. Laird, *J. Chem. Phys.* 118 (2003) 7651.
- [15] X.-M. Bai, M. Li, *J. Chem. Phys.* 124 (2006) 124707.
- [16] Y. Shibuta, T. Suzuki, *Chem. Phys. Lett.* 498 (2010) 323.
- [17] Y. Watanabe, Y. Shibuta, T. Suzuki, *ISIJ Int.* 50 (2010) 1158.
- [18] Y. Shibuta, Y. Watanabe, T. Suzuki, *Chem. Phys. Lett.* 475 (2009) 264.
- [19] J. Hoyt, M. Asta, A. Karma, *Phys. Rev. Lett.* 86 (2001) 5530.
- [20] D. Sun, M. Asta, J. Hoyt, *Phys. Rev. B* 69 (2004) 024108.
- [21] D. Sun, M. Asta, J. Hoyt, *Phys. Rev. B* 69 (2004) 174103.
- [22] D. Sun, M. Mendelev, C. Becker, K. Kudin, T. Haxhimali, M. Asta, J. Hoyt, A. Karma, D. Srolovitz, *Phys. Rev. B* 73 (2006) 024116.
- [23] J. Hoyt, M. Asta, *Phys. Rev. B* 65 (2002) 214106.
- [24] K. Christmann, *Surf. Sci. Rep.* 9 (1988) 1.
- [25] M. Amini, B.B. Laird, *Phys. Rev. B* 78 (2008) 144112.
- [26] M. Amini, B.B. Laird, *Phys. Rev. Lett.* 97 (2006) 216102.
- [27] R.L. Davidchack, J.R. Morris, B.B. Laird, *J. Chem. Phys.* 125 (2006) 094710.
- [28] H. Zhou, X. Lin, M. Wang, W. Huang, *J. Cryst. Growth* 366 (2013) 82.
- [29] H. Zhou, X. Lin, M. Wang, W. Huang, *J. Cryst. Growth* 377 (2013) 107.
- [30] J. Liu, R. Davidchack, H. Dong, *Comput. Mater. Sci.* 74 (2013) 92.
- [31] M.S. Daw, M.I. Baskes, *Phys. Rev. Lett.* 50 (1983) 1285.
- [32] M.S. Daw, M.I. Baskes, *Phys. Rev. B* 29 (1984) 6443.
- [33] M.S. Daw, S.M. Foiles, M.I. Baskes, *Mater. Sci. Rep.* 9 (1993) 251.
- [34] M. Baskes, *Phys. Rev. Lett.* 59 (1987) 2666.
- [35] M. Baskes, *Phys. Rev. B* 46 (1992) 2727.
- [36] B.-J. Lee, J.-H. Shim, M. Baskes, *Phys. Rev. B* 68 (2003) 144112.
- [37] J.-M. Zhang, F. Ma, K.-W. Xu, *Appl. Surf. Sci.* 229 (2004) 34.
- [38] E. Asadi, M.A. Zaeem, A. Moitra, M.A. Tschopp, *J. Phys. Condens. Matter* 26 (2014) 115404.
- [39] B.-J. Lee, M. Baskes, H. Kim, Y.K. Cho, *Phys. Rev. B* 64 (2001) 184102.
- [40] M. Baskes, R. Johnson, *Modell. Simul. Mater. Sci. Eng.* 2 (1994) 147.
- [41] W. Hu, B. Zhang, B. Huang, F. Gao, D.J. Bacon, *J. Phys. Condens. Matter* 13 (2001) 1193.
- [42] J.M. Zhang, F. Ma, K.W. Xu, X.T. Xin, *Surf. Interface Anal.* 35 (2003) 805.
- [43] B. Jelinek, S. Groh, M. Horstemeyer, J. Houze, S. Kim, G. Wagner, A. Moitra, M. Baskes, *Phys. Rev. B* 85 (2012) 245102.
- [44] E. Asadi, M.A. Zaeem, S. Nouranian, M.I. Baskes, *Phys. Rev. B* (2014), In press, <http://dx.doi.org/10.1103/PhysRevB.00.004100>.
- [45] S. Nouranian, M.A. Tschopp, S.R. Gwaltney, M.I. Baskes, M.F. Horstemeyer, *Phys. Chem. Chem. Phys.* 16 (2014) 6233.
- [46] J.H. Rose, J.R. Smith, F. Guinea, J. Ferrante, *Phys. Rev. B* 29 (1984) 2963.
- [47] J.A. Zimmerman, H. Gao, F.F. Abraham, *Modell. Simul. Mater. Sci. and Eng.* 8 (2000) 103.
- [48] G. Simmons, H. Wang, *Single Crystal Elastic Constants and Calculated Aggregate Properties*, Massachusetts Institute of Technology, Cambridge, MA, 1971.
- [49] H.E. Schaefer, R. Gugelmeier, M. Schmolz, A. Seeger, *Positron lifetime spectroscopy and trapping at vacancies in aluminium*, Materials Science Forum, vol. 15, TransTech, Zurich, Switzerland, 1987, p. 111.
- [50] W. Schüle, *Z. Metallkd* 89 (1998) 672.
- [51] W. Wycisk, M. Feller-Kniepmeier, *J. Nucl. Mater.* 69/70 (1978) 616.
- [52] A.T. Dinsdale, *Calphad* 15 (1991) 317.
- [53] C.S. Barrett, T.B. Massalski, *Structure of Metals*, McGraw-Hill, New York, 1966.
- [54] W. Tyson, W. Miller, *Surf. Sci.* 62 (1977) 267.
- [55] W.F. Gale, T.C. Totemeier, *Smithells Metals Reference Book*, Butterworth-Heinemann, Oxford, 2003.
- [56] W.M. Haynes, *CRC Handbook of Chemistry and Physics*, CRC Press, Boca Raton, FL, 2012.
- [57] A. James, M. Lord, *Macmillan's Chemical and Physical Data*, Macmillan, London, 1992.

- [58] J.G. Speight, Lange's Handbook of Chemistry, McGraw-Hill, New York, 2005.
- [59] S. Plimpton, J. Comput. Phys. 117 (1995) 1.
- [60] Y. Waseda, The Structure of Non-Crystalline Materials: Liquids and Amorphous Solids, McGraw-Hill, New York, 1980.
- [61] E. Lorch, J. Phys. C Solid State Phys. 2 (1969) 229.
- [62] J. Hoyt, M. Asta, A. Karma, Interface Sci. 10 (2002) 181.
- [63] S. Nosé, J. Chem. Phys. 81 (1984) 511.
- [64] W.G. Hoover, Phys. Rev. A 31 (1985) 1695.
- [65] A. Karma, Phys. Rev. E 48 (1993) 3441.
- [66] W. Fehrlner, S. Vosko, Can. J. Phys. 54 (1976) 2159.
- [67] Q. Jiang, H. Lu, Surf. Sci. Rep. 63 (2008) 427.
- [68] M. Gündüz, J. Hunt, Acta Metall. 33 (1985) 1651.
- [69] L. Gránásy, M. Tegze, A. Ludwig, Mater. Sci. Eng. A 133 (1991) 577.